

Comprehending the potential correlation between strain performances and phase boundary characteristics of BNT-based systems

Xiaojun Wu¹, Chao Wu¹, Lanji Wen¹, Jie Yin^{1,2,*} and Jiagang Wu^{1,†}

¹College of Materials Science and Engineering, Sichuan University, Chengdu 610064, People's Republic of China

²Institute of Materials Research and Engineering (IMRE), Agency for Science, Technology and Research, Singapore, Republic of Singapore



(Received 3 December 2023; accepted 27 February 2024; published 21 March 2024)

$\text{Bi}_{0.5}\text{Na}_{0.5}\text{TiO}_3$ (BNT)-based systems are potential candidates for actuators due to their outstanding strain performances. Despite various doping components having been utilized to regulate their strain performances, the systematical route for designing giant-strain BNT-based materials remains elusive. Herein, we decode the potential correlation between strain performances and phase boundary characteristics and then propose a complete guideline for designing BNT-based materials with the giant strain. Since the polarization rotation is closely correlated to the phase transition process, the morphology phase boundary (MPB) frame of initial BNT matrix can maintain its partial properties for the polarization rotation, when introducing bits of doping components to tailor the transition temperature. The screened K6LT matrix with the optimized MPB frame exhibits a d_{33} of 260 pC/N, and the $(\text{Zr}_{0.5}\text{Nb}_{0.5})$ -modified K6LT matrix (K6LT-ZN1) exhibits a low driving field $E_{\text{pol}} \sim 38.4$ kV/cm and high large-signal piezoelectric coefficient $d_{33@60}^* \sim 727$ pm/V. This proposed design guideline reveals the significance for BNT matrix screening and could be a feasible method for constructing BNT-based systems with excellent strain performances.

DOI: [10.1103/PhysRevMaterials.8.034406](https://doi.org/10.1103/PhysRevMaterials.8.034406)

I. INTRODUCTION

Over the past years, lead-free ferroelectric materials have been a popular topic in ferroelectric research [1,2]. Among typical lead-free ferroelectrics [$\text{K}_{0.5}\text{Na}_{0.5}\text{NbO}_3$ (KNN), BaTiO_3 (BT), and $\text{Bi}_{0.5}\text{Na}_{0.5}\text{TiO}_3$ (BNT)], BNT is considered as the potential candidate for green actuators [3]. Currently, the prevailing theory believes that the reversible ergodic relaxor-ferroelectric transition triggers excellent strain performances (giant and reversible strain) in BNT-based materials [1,4]. Therefore, regulating the ferroelectric-relaxor temperature (T_{f-r}) and optimizing constituent phase transition are crucial factors in attaining a significant strain [4,5].

According to the classical relaxor theory, the random-field effect (random elastic and electric field) can disrupt long-range ferroelectric orders and then induce the relaxation characteristics [4,6]. Hence, strain regulation methods (such as chemical substitution) referring to tailor the transition temperature should only rely on the random-field effect. The random-field effect shifts T_{f-r} to an appropriate temperature for the relaxor-ferroelectric transition, which is the precondition for excellent strain performances. In other words, it only ensures the occurrence of a unique strain [4,7]. There is no doubt that the unique strain is larger than general strain caused by the domain-wall motivation, piezoelectric effect and electrostriction, while existing strain-level discrepancies among different BNT-based materials cannot be

ignored [e.g., large-signal piezoelectric coefficient d_{33}^* and d_{33}^* of BaZrO_3 -modified BNT ~ 500 pm/V and d_{33}^* of BaSnO_3 -modified BNT- BaTiO_3 (BNBT) ~ 669 pm/V] [7–9]. The strain level of this unique strain should be dominated by the constituent relaxor-ferroelectric transition process, including lattice structural discrepancies (between relaxors and ferroelectrics) and phase transition state [1,4,10]. Theoretically, enhancing structural discrepancies is beneficial for improving the strain level, whereas it demands to conceive giant electric field-induced structural discrepancies with almost no hints and trial-and-error experiments are inevitable. Moreover, considering the local structural heterogeneity and complex competition relation (multiple cations coexist in the same position) [11,12], the lattice structure of BNT-based relaxors is challenging to be quantitatively defined, let alone the precise characterization of structural discrepancies [13–16]. Thus, optimizing the phase transition state (e.g., driving field and transition degree) to improve strain performances is more reasonable.

In essence, the ferroelectric phase transition indicates the switching among stable energy states, and the underlying frame of any phase transition process referred to ferroelectrics is transformed polarization vectors [17]. Decreasing the energy barriers with the flattened Gibbs energy curve and eased polarization rotation is the intuitional method to facilitate the phase transition process and achieve a giant strain [12,18]. Morphology phase boundary (MPB), a milestone conception of the ferroelectric development history, which can optimize the ferroelectricity (piezoelectricity) via decreasing energy barriers and easing polarization rotation processes, fits the demand perfectly [18,19]. Employing the MPB and

*Corresponding author: m15608012851@163.com

†Corresponding author: wujiagang0208@163.com

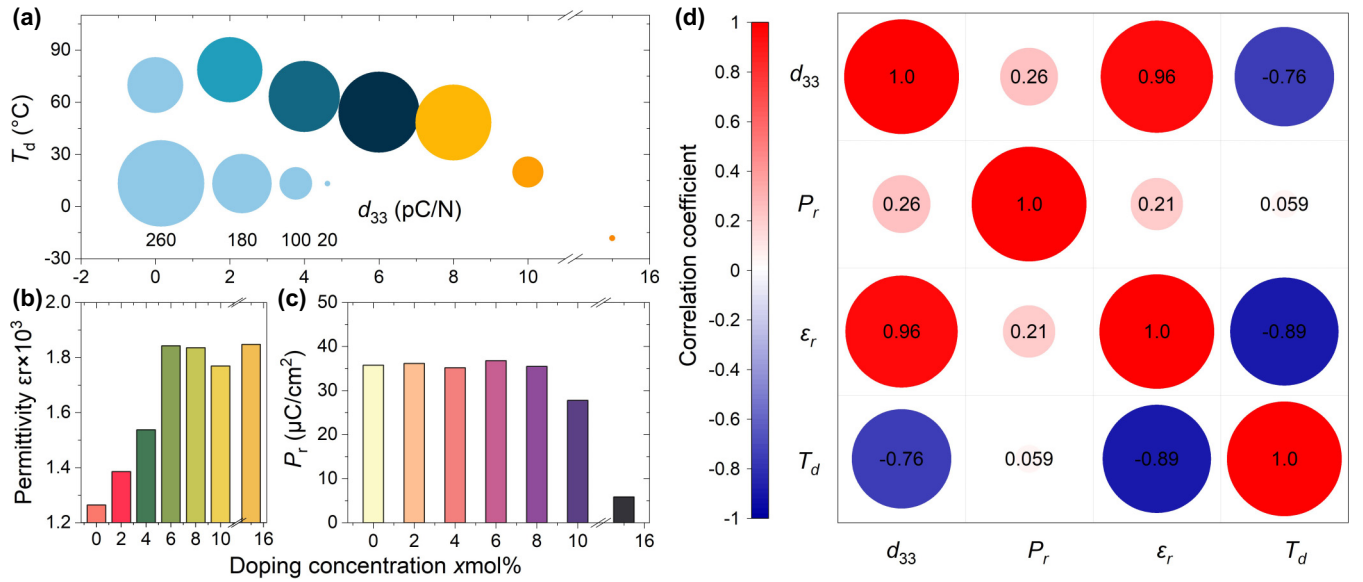


FIG. 1. (a)–(c) Piezoelectric, dielectric (RT), and remanent polarization performances of K100xLT samples ($x = 0 \sim 0.15$). (d) Correlation analysis for piezoelectricity and ferroelectric–dielectric properties (K100xLT, $x = 0 \sim 0.08$).

constructing a crossover of relaxor–MPB are believed to achieve a giant strain in BNT-based materials, and a recent phase-field simulation result confirms the feasibility of this design [20]. Now, the remaining issue is *how to construct the MPB–relaxor crossover*. Doping components can shift the T_{f-r} to room temperature (RT) via the mentioned random-field effect, while introduced doping components will inevitably change the initial phase structure. This variation is hard to predict, and more importantly, the final phase structure cannot be precisely determined (e.g., whether the final phase structure possesses an excellent MPB frame). To solve this question, by analogy with piezoelectricity optimization ways of perovskite ferroelectrics KNN and $\text{Pb}(\text{Zr},\text{Ti})\text{O}_3$ (PZT) (i.e., chemical doping is generally employed in a matrix with relatively excellent electromechanical properties) [8,21–26], we take the following guideline, that is, selecting a BNT matrix with an optimal MPB frame and employing chemical substitution to shift the transition temperature based on the matrix. Note that the applied doping components should be highly efficient for regulating the transition temperature; otherwise, the phase structure will deviate excessively.

Herein, we construct a type of BNT matrix $[\text{Bi}_{0.5}(\text{Na}_{0.8-x}\text{K}_{0.2}\text{Li}_x)_{0.5}\text{TiO}_3$, $x = 0, 0.02, 0.04, 0.06, 0.08, 0.10$, and 0.15 , abbreviated as KT ($x = 0$) and K100xLT] with excellent piezoelectric properties (K6LT, piezoelectric coefficient $d_{33} \sim 260$ pC/N). Complexed B-site ions ($\text{Zr}_{0.5}\text{Nb}_{0.5}$) are introduced to tailor the T_{f-r} of $\text{Bi}_{0.5}(\text{Na}_{0.8-x}\text{K}_{0.2}\text{Li}_x)_{0.5}\text{Ti}_{1-y}(\text{Zr}_{0.5}\text{Nb}_{0.5})_y\text{O}_3$, $x = 0(0.06)$, $y = 0.005, 0.01, 0.015, 0.02$ and 0.03 , abbreviated as KT(K6LT)–ZN100y. See more experimental details in the Supplemental Material [27]. The K6LT–ZN1 exhibits a high strain value with $d_{33@60}^*$ (the subscript @60 corresponds to the testing field 60 kV/cm) of 727 pm/V, much larger than typical piezoelectric materials (e.g., soft PZT PIC151 ~ 500 pm/V, PZT-4 ~ 410 pm/V, BiFeO_3 -modified BT ~ 375 pm/V, KNN ~ 150 pm/V, and BiFeO_3 -modified KNN ~ 505 pm/V)

[1,28–31]. However, the $d_{33@60}^*$ of ($\text{Zr}_{0.5}\text{Nb}_{0.5}$)-modified KT ($d_{33} \sim 180$ pC/N) only reaches 583 pm/V. The significant enhancement of d_{33}^* confirms the plausibility of the proposed design routine. Certainly, it cannot be denied that doping components occasionally regulate the initial MPB frame to the more appropriate situation, leading to the higher strain than that in the BNT matrix with an optimized MPB. In other words, the proposed guideline provides a more efficient method for designing BNT-based materials with excellent strain performances, rather than relying on the trial-and-error experiments.

II. RESULTS AND DISCUSSION

A. Optimizing the MPB frame of BNT matrix

First, some influential factors (e.g., impurities and grain state) are excluded to ensure the reliability of experiments prior to characterizing electrical properties of K100xLT samples (Figs. S1 and S2 [27]).

Then, piezoelectric properties of K100xLT samples are collected in Fig. 1(a). The depolarization temperature (T_d) is extracted from the transition temperature T_{f-r} from ϵ_r - E curves (Fig. S3 [27]) considering the slight value discrepancy, and for poled K100xLT samples with no ferroelectric-relaxor transition peaks, the *Vogel-Fulcher* relation (Fig. S4 [27]) is applied to calculate the freezing temperature (T_f) that equals to T_d [6].

Overall, the piezoelectric coefficient (d_{33}) gradually increases with the increasing Li^+ contents, while when $x \geq 0.10$, the d_{33} shows a drastic decrease due to the low T_d ($< \text{RT}$). The K6LT sample exhibits the most excellent piezoelectric performances ($d_{33} \sim 260$ pC/N, $T_d \sim 54.2^\circ\text{C}$), whereas the primary piezoelectricity optimization mechanism cannot be arbitrarily attributed to the optimized MPB frame with facile domain-wall motion and polarization rotation, given that some relevant factors (i.e., intrinsic lattice distortion,

grain-size effect) for improving piezoelectricity are not excluded [32,33]. Therefore, prior to further composition modification for tailoring the transition temperature and strain performances, decoding the constituent piezoelectricity optimization mechanism is critical, which will also be helpful to support the rounded technical route (guideline) for achieving excellent strain performances in BNT-based systems.

B. Mechanism for optimized piezoelectric performances: Domain-wall dynamics

Based on the electrostriction and piezoelectric tensor formula (i.e., $S_{ij} = Q_{ijkl}P_kP_l$ and $d_{mij} = \partial S_{ij}/\partial E_m$), the piezoelectric coefficient can be eventually expressed as $d_{ijk} = Q_{ijkl}P_k\varepsilon_{lm} + Q_{ijkl}P_l\varepsilon_{km}$, presenting a close correlation with electrostrictive coefficient Q , polarization P , and permittivity ε . The electrostriction arises from the pair potential anharmonicity, and the fluctuation of Q is generally limited (<5%) due to confined ion displacements in the same perovskite system (e.g., BNT). [34] Hence, usually it is only to consider contributions from P and ε for a piezoelectricity variation. In more detail, for a quasistatic d_{33} characteristic, the polarization and permittivity should be remanent polarization (P_r) and zero-field-RT permittivity, respectively.

The zero-field-RT permittivity [Fig. 1(b)] is extracted from dielectric curves (Figs. S3 and S4 [27]), and the remanent polarization [Fig. 1(c)] is extracted from polarization hysteresis loops (Fig. S5 [27]). Herein, we only focus on disentangling the correlation among polarization, permittivity, and piezoelectricity for K100xLT ($x = 0 \sim 0.08$) with a T_d above RT regardless of some parameter transformations (e.g., drastically decreasing P_r) for high doping components (K10LT and K15LT) due to the low T_d (<RT). The P_r only exhibits slight fluctuations among K100xLT ($x = 0 \sim 0.08$) (e.g., P_r of KT $\sim 35.8 \mu\text{C}/\text{cm}^2$ and P_r of K6LT $\sim 36.8 \mu\text{C}/\text{cm}^2$), while obvious improvement of ε_r can be observed from KT to K6LT, revealing that the enhanced d_{33} performance arises from the reinforced small-signal permittivity rather than large-signal P_r . The correlation analysis [Fig. 1(d)] among d_{33} , P_r , ε_r , and T_d further confirms the close relation between permittivity and piezoelectricity (i.e., the correlation coefficient for ε_r and d_{33} is 0.96, while it is 0.26 for P_r and d_{33}).

So far, the remaining question is *what causes the enhanced permittivity?* For ferroelectric single crystal, the permittivity only includes contributions from intrinsic lattice distortion and extrinsic domain-wall motion; however, the intergranular coupling effect should be realized when involved in ferroelectric polycrystalline ceramics [33,35]. Most grain effects (e.g., grain-size effect and grain-boundary effect) are considered as internal stress-dependent effects, regulating the Gibbs energy profile and polarization states via the internal stress [32]. Interestingly, these effects will be weakened in relaxors due to the existence form of relaxor units (i.e., high density of low-angle domain-walls or nonpolar matrix + nanosized polar regions) [12]. Moreover, similar grain morphologies with finite grain-size variation are found in KT and K6LT, further demonstrating that the intergranular effect is not the primary factor for the enhanced permittivity.

Regarding the intrinsic lattice contribution, the Raman spectra are utilized to characterize the atomic-scale lattice

deviation via phonon mode variations (Fig. S6 [27]). Samples with different doping concentration (from KT to K6LT to K15LT) possess the similar Raman spectra shape, and no significant distortions of phonon vibration modes are observed. These phenomena indicate restricted direct polarization variations from the changed atomic–electronic–dipole orientation displacement caused by the chemical substitution (i.e., KT, K6LT, and K15LT). In fact, lattice discrepancies in the same perovskite system (BNT system) are generally restricted due to the definite perovskite tolerator frontiers related to structure stability, and so small-signal electrical parameters (e.g., d_{33} and ε_r) are primarily affected by some indirect factors, for instance, domain-wall dynamics [34]. Note that the lattice structure eventually determines macroscopic electrical characteristics and so these indirect factors should also be structure driven (e.g., lattice distortion induces the softened lattice with reinforced domain-wall dynamics and polarization rotation) [36].

Before delving into the correlation between lattice evolution and domain-wall dynamics, it is imperative to confirm whether domain-wall dynamics indeed govern the heightened permittivity and piezoelectric characteristics. Hence, the *in situ* ε_r - E and $\tan \delta$ - E are characterized in Figs. 2(a) and 2(b). The permittivity exhibits an increasing trend with the increasing doping contents, conforming to dielectric measurements, whereas the loss peak value gradually decreases from KT to K15LT, which implies two possibilities: (i) the weakened domain-wall motion ability with low electromechanical performances and (ii) the changed domain-wall state and motion characteristics with optimized electromechanical performances. Combining with the piezoelectricity transformations from KT to K6LT, there is no doubt that the decreasing loss peak value should be attributed to the changed domain-wall dynamic characteristics [35]. In fact, inner polar entities of relaxors can be consciously distributed as the mode, high density of low-angle domain wall, which is beneficial for domain-wall motion (e.g., decreasing motivation activation energy) [12,36]. The increasing doping contents accompanied with enhanced random-field effect will trigger the reinforced relaxation properties in K100xLT samples, and then the higher domain-wall density with lower domain-wall angle results in the stronger domain-wall dynamics while lower motion loss. Mesoscopic domain morphologies [Fig. 2(i)] confirm the decreasing domain size and increasing domain-wall density from KT to K6LT.

Polarization hysteresis loops under the subswitching-field condition [Fig. 2(c)] are employed to further investigate domain-wall dynamics characteristics of KT and K6LT. The P_r of K6LT under the subswitching-field condition (P_r^{sub}) is close to that of KT due to activated polar entities with enhanced reversibility. The maximum polarization (P_{max}) of K6LT under the subswitching-field condition ($P_{\text{max}}^{\text{sub}}$) exhibits obvious enhancement compared with that of KT [Fig. 2(d)], corresponding to the enhanced permittivity (the slope for $P_{\text{max}}^{\text{sub}}$ - E evolution). Moreover, the $P_{\text{max}}^{\text{sub}}$ - E slope gradually increases with the increasing electric field, demonstrating the extrinsic domain-wall motion indeed contributes to dielectric performances [37]. Typically, as for predicting and analyzing nonlinear behaviors of ferroelectrics, Rayleigh law (RL) is the preferred mode [32,34]. And, considering

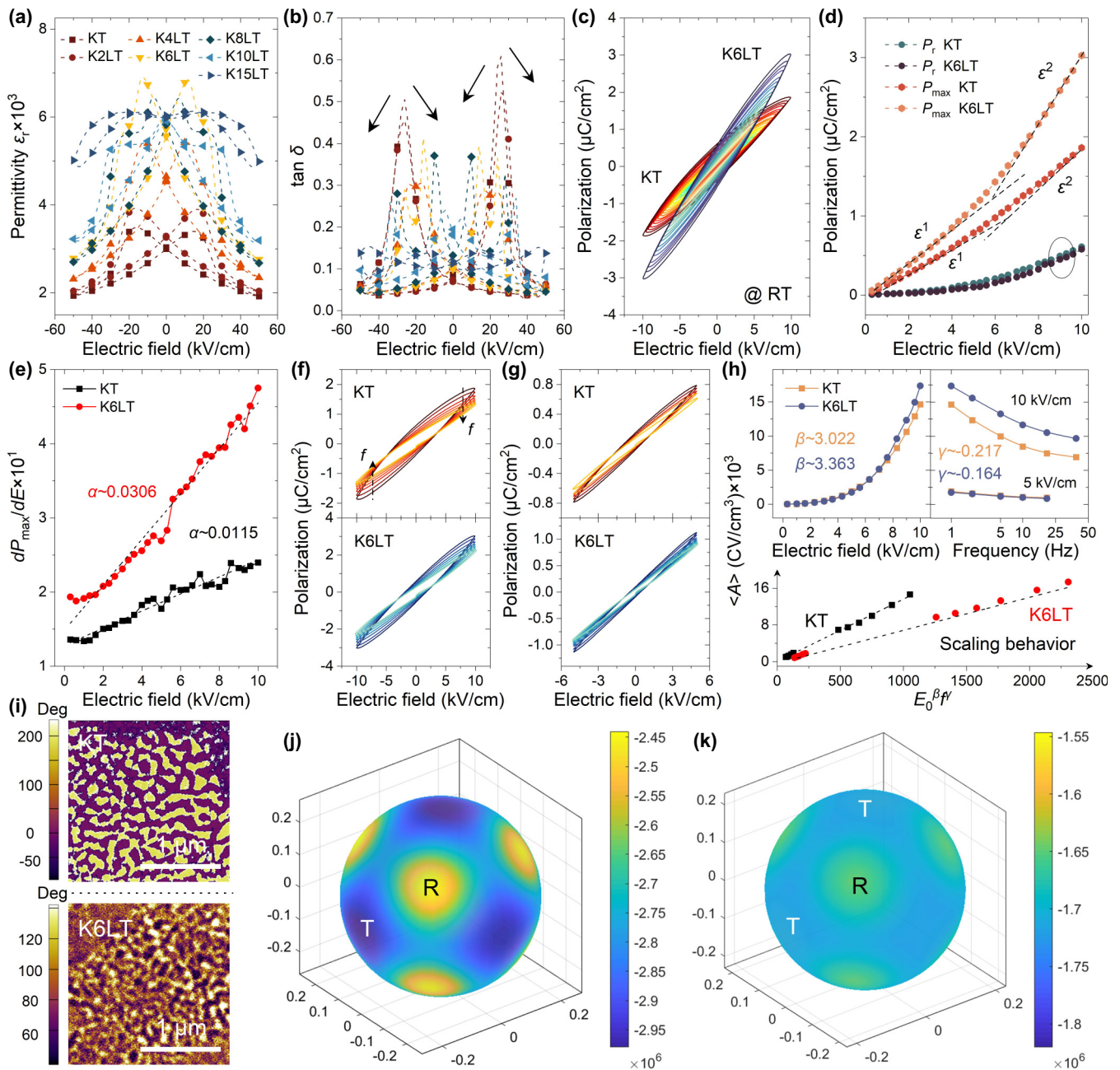


FIG. 2. (a), (b) *In situ* permittivity (ϵ_r - E) and loss ($\tan \delta$ - E) loops of K100xLT samples. (c) Polarization hysteresis loops of KT and K6LT samples under the subswitching field. (d) P_r and P_{\max} evolution under the subswitching field. (e) Rayleigh analysis for KT and K6LT samples. (f)–(h) Power-law analysis for domain-wall dynamics characteristics of KT and K6LT samples. (i)–(k) Mesoscopic domain characteristics and Gibbs energy simulation results of the of KT and K6LT samples.

the similar situation for MPB and RL (i.e., for MPB, multicoexisting and disordering polarization state; for RL, the potential set by pinning centers is distributed in a perfect random fashion) [37], RL should be appropriate for decoding domain-wall dynamics characteristics of KT and K6LT.

According to the RL expression for the dielectric response [35,37]: $\epsilon'(E) = \epsilon'_{\text{init}} + \alpha E$, where ϵ'_{init} represents the intrinsic lattice contribution and reversible domain-wall contribution, and α is the RL coefficient related to nonlinear

behaviors, it can be found that the RL coefficient α of K6LT is about 0.0306 [Fig. 2(e)] which is nearly three times than α of KT (0.0115). The higher nonlinear coefficient indicates the stronger domain-wall dynamics characteristics and then dedicates to the improved small-signal electrical parameters (e.g., d_{33} and ϵ_r) of K6LT.

Besides the commonly used RL model, the scaling behavior among hysteresis area $\langle A \rangle$, remanent polarization P_r , frequency f , and electric field E can supply more detailed information about domain-wall dynamics (e.g., domain-wall

motion, switching, and nucleation growth dynamics) [38]. According to the scaling relationship (i.e., $\langle A \rangle \propto E^\beta f^\gamma$, where β represents the domain motion ability following the external field direction, and γ refers to the required domain response time under the external field) [39,40], we first plotted $\langle A \rangle$ against E at the fixed f to determine the parameter β [Figs. 2(h) and 2(c)], and then similar method is utilized to determine the exponent γ [Figs. 2(f)–2(h)]. The scaling behavior of KT and K6LT in the range of frequency from 1 to 40 Hz [Figs. 2(f) and 2(g)] and electric field from 0.33 to 10 kV/cm [Fig. 2(c)] can be finally expressed as $\langle A \rangle \propto E^{3.022} f^{-0.217}$ and $\langle A \rangle \propto E^{3.363} f^{-0.164}$, respectively [Fig. 2(h)]. Compared to KT, the higher β but lower γ of K6LT reveals the stronger following ability (along external electric field) and quicker response process for the domain-wall motion, further illustrating the enhanced domain-wall dynamics performances of K6LT.

So far, it can be concluded that the reinforced domain-wall dynamics characteristics (i.e., domain-wall motion ability and response time) with the facilitated polarization rotation process are the primary factors for enhanced piezoelectric performances. Next, we will *elucidate the relation between domain-wall dynamics and MPB frame*. Regarding domain-wall dynamics of polycrystalline ferroelectric ceramics, influential factors can be classified to the lattice structure (from a larger view, the lattice structure refers to the MPB frame) and intergranular effect. And, as mentioned above, grain effects (grain size and boundary effect) on polarization fluctuations can be generally neglected for relaxors due to the particularity of relaxor units. Therefore, the variations of domain-wall dynamics directly reflect the changed MPB frame, and the optimized MPB frame should be responsible for reinforced domain-wall dynamics of K6LT. Phase-field simulation results of the Gibbs energy (i.e., the K6LT exhibits the flatter energy curve with a lower rhombohedral-tetragonal (R - T) energy barrier than KT) also verify the optimized MPB frame of K6LT.

C. Mechanism for optimized piezoelectric performances: Phase component and lattice structure

To guide the design of appropriate MPB frames with the facile polarization rotation, the phase component and atomic-scale lattice evolution are explored. The x-ray-diffraction patterns for poled K100xLT ($x = 0, 0.02, 0.06, 0.10,$ and 0.15), samples are presented in Fig. 3(a) with local amplified images about perovskite characteristic diffraction peaks (111) and (200). With the increasing doping contents, the split (111) diffraction peak gradually merges, while the (200) diffraction peak remains split, indicating the decreasing rhombohedral phase ratio and increasing tetragonal phase ratio [15]. Rietveld refinement is employed to further investigate the phase component [right of Fig. 3(a)], based on the $R3c + P4bm$ model. From KT to K15LT, the $R3c$ proportion decreases from 76.7 to 24.9%, and the $P4bm$ proportion increases from 23.3 to 75.1%. This conforms to the qualitative judgment based on variations in diffraction-peaks (111) and (200). The optimal composition K6LT presents the phase component of $R3c \sim 57.4\%$ and $P4bm$ 42.6%, indicating that an unbalanced phase ratio (i.e., slightly more $R3c$ and less $P4bm$) should

be appropriate for optimizing the MPB frame of BNT-based systems.

In essence, the changed phase component arises from atomic-scale lattice distortions, and the B -site atom deviation and BO_6 octahedral distortion dominate the polarization for typical perovskite systems (e.g., KNN, BT, and BNT). Raman spectra (Fig. S6 [27]) are employed to initially analyze the atomic-scale lattice evolution. For Raman spectra of BNT-based systems, vibration modes ranging from 150 to 450 cm^{-1} (above 450 cm^{-1}) are linked with Ti-O vibrations and breathing (stretching) modes of BO_6 octahedral, respectively [41]. According to Lorentz simulation results [Fig. S7 and Fig. 3(b) [27]] from KT to K15LT, the Ti–O bond length first increases and then decreases, accompanied with the gradually transformed octahedral torsion mode. Ti K -edge x-ray absorption spectroscopy spectra [Figs. 3(c)–3(e)] give more plausible information about the Ti-dependent–TiO₆ distortion. The peak position (shape) of $1s - 3d(4p)$ electronic transition is mainly correlated with the valent of Ti ions, and the peak intensity of $1s - 3d$ electronic transition is correlated with oxygen octahedral distortion [42]. As shown, all the samples present a similar peak position (shape), indicating the identical valent of Ti ions. The major difference among KT, K6LT and K15LT is reflected in the peak intensity of $1s - 3d$ electronic transition. More specifically, K6LT presents the strongest intensity, and KT (K15LT) presents the medium (weakest) intensity, respectively. Fourier transform (FT) of extended x-ray absorption fine structure (EXAFS) spectra [Fig. 3(e)] further reveals Ti-dependent chemical bond (i.e., Ti–O and Ti–Ti) information, making these microscopic structure transformations more concrete and visual. The Ti–Ti bond length is almost unchanged for different doping concentrations, whereas K6LT exhibits the slight increase of Ti–O bond length compared with KT (K15LT). To sum up, the discrepant structure parameters (e.g., chemical bond parameters and oxygen octahedral torsion mode) can regulate the polarization transformation situation towards different trends, and the structure state of BNT-based systems, that is, stretched lattice with intense noncentrosymmetric oxygen octahedral, is beneficial for optimizing MPB frame, thereby decreasing the polarization rotation barriers and improving the domain-wall migration. Herein, it should be stressed again that the direct polarization enhancement from lattice distortions is limited, and lattice distortions tailor dielectric–piezoelectric–ferroelectric performances by regulating the MPB frame and domain-wall dynamics.

D. Strain properties for different BNT-based systems

Giant- and reversible strain properties of BNT-based systems arise from the ergodic relaxor-ferroelectric transition, and so we regulate the T_d of screened matrix K6LT to RT by the heterovalent (heteroradius) ion-triggered random-field effect [($Zr_{0.5}Nb_{0.5}$) doping] [4]. The ($Zr_{0.5}Nb_{0.5}$) doping is also introduced into the initial matrix KT to serve as the control experiment.

Some interference factors for electrical characterizations are first excluded, including the impurity (Fig. S8 [27]) and grain-size effect (Figs. 4(a) and Fig. S9 [27]). Then, the T_f (equals to T_d) of KT-ZN100 y and K6LT-ZN100 y (Figs. 4(b)

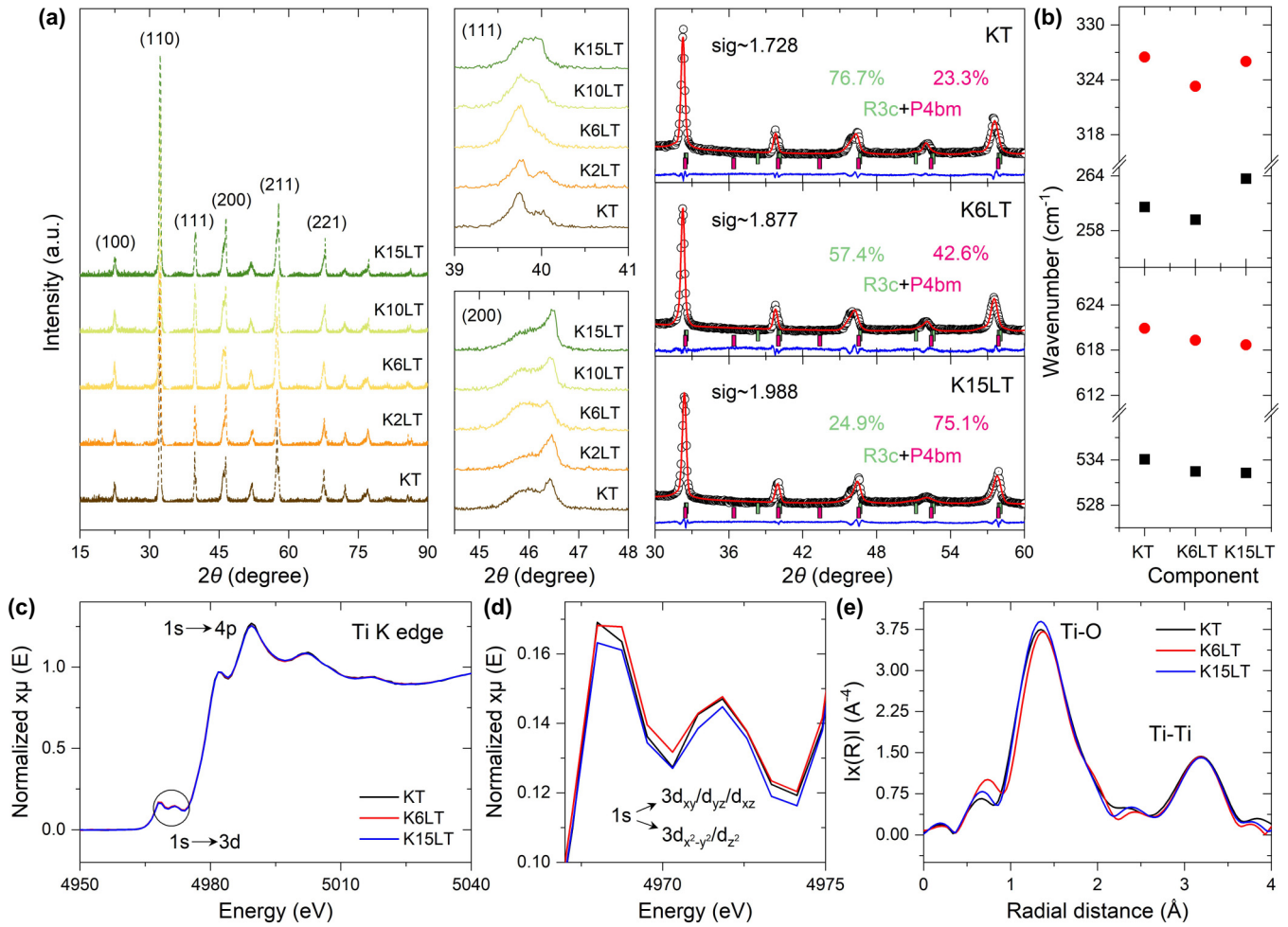


FIG. 3. (a) X-ray-diffraction patterns of poled K100 \times LT ($x = 0, 0.02, 0.06, 0.10$ and 0.15) samples in the range of $15^\circ - 90^\circ$ and the Rietveld refinement of KT, K6LT and K15LT samples. (b) Lorentz simulation results for Raman spectra. (c) Normalized Ti K-edge x-ray absorption near-edge structure (XANES) spectra of KT, K6LT and K15LT samples. (d) Local amplified spectra for electronic transition $1s - 3d$. (e) FT-transformed Ti K-edge extended x-ray absorption fine structure (EXAFS) spectra of KT, K6LT and K15LT samples.

and 4(c) and Figs. S10 and S11 [27]) are calculated to filtrate the potential appropriate composition (T_f close to RT) for giant-strain properties. Possibly caused by the close initial depolarization temperature (T_d for KT $\sim 69.8^\circ\text{C}$ and for K6LT $\sim 54.2^\circ\text{C}$), the critical compositions for KT and K6LT matrix present the identical ($Zr_{0.5}Nb_{0.5}$)-doping concentrations (i.e., KT (K6LT)-ZN1 and KT (K6LT)-ZN1.5). This inadvertent move further refines the control group (the first group: KT-ZN1 and K6LT-ZN1; the second group: KT-ZN1.5 and K6LT-ZN1.5) and enhances the coherence of control groups.

Strain performances (strain-hysteresis loop, S - E) of KT (K6LT)-ZN1 and KT (K6LT)-ZN1.5 under the testing electric field 60 (70) kV/cm are exhibited in Figs. 4(e) and Fig. 4(f), respectively. Strain performances of the other samples are shown in Fig. S12 [27]. For the first control group, K6LT-ZN1 exhibits more significant enhancement of strain levels than KT-ZN1 under the testing field of 60 kV/cm (maximum of strain $S_{\max@60}$ and $d_{33@60}^*$ of K6LT-ZN1 $\sim 0.44\%$, 727 pm/V; KT-ZN1 $\sim 0.35\%$, 583 pm/V; the subscript @60 corresponds to the testing field 60 kV/cm), while the strain discrepancy decreases under the testing field of 70 kV/cm ($S_{\max@70}$ and

$d_{33@70}^*$ of K6LT-ZN1 $\sim 0.47\%$, 664 pm/V; KT-ZN1 $\sim 0.43\%$, 615 pm/V; the subscript @70 corresponds to the testing field 70 kV/cm). By evaluating the poling field E_{pol} (driving field) level [Figs. 4(e) and 4(g)] that is extracted from the inflection point of the S - E loop (strain-hysteresis loop), it is easy to predict that the former (enhanced $d_{33@60}^*$ of K6LT-ZN1) should be attributed to the obviously decreasing poling field of K6LT-ZN1 (E_{pol} of K6LT-ZN1 ~ 38.4 kV/cm; KT-ZN1 ~ 50.2 kV/cm), whereas the latter (decreased strain discrepancy $S_{\max@70}/d_{33@70}^*$ between KT-ZN1 and K6LT-ZN1) may be correlated with two factors: (i) the relatively high driving field of KT-ZN1 and (ii) lattice discrepancies between the initial relaxors and eventually ferroelectric state. Herein, we first focus our attention on the driving-field variations, considering the constituent relationship among MPB, phase transition, and strain performances (i.e., MPB frame is correlated with the polarization rotation-phase transition process and then regulates the driving field and strain performances) [1,26]. The obviously decreasing poling field of K6LT-ZN1 reveals that without excessive doping contents to tailor the depolarization temperature, the optimized MPB frame of initial matrix can

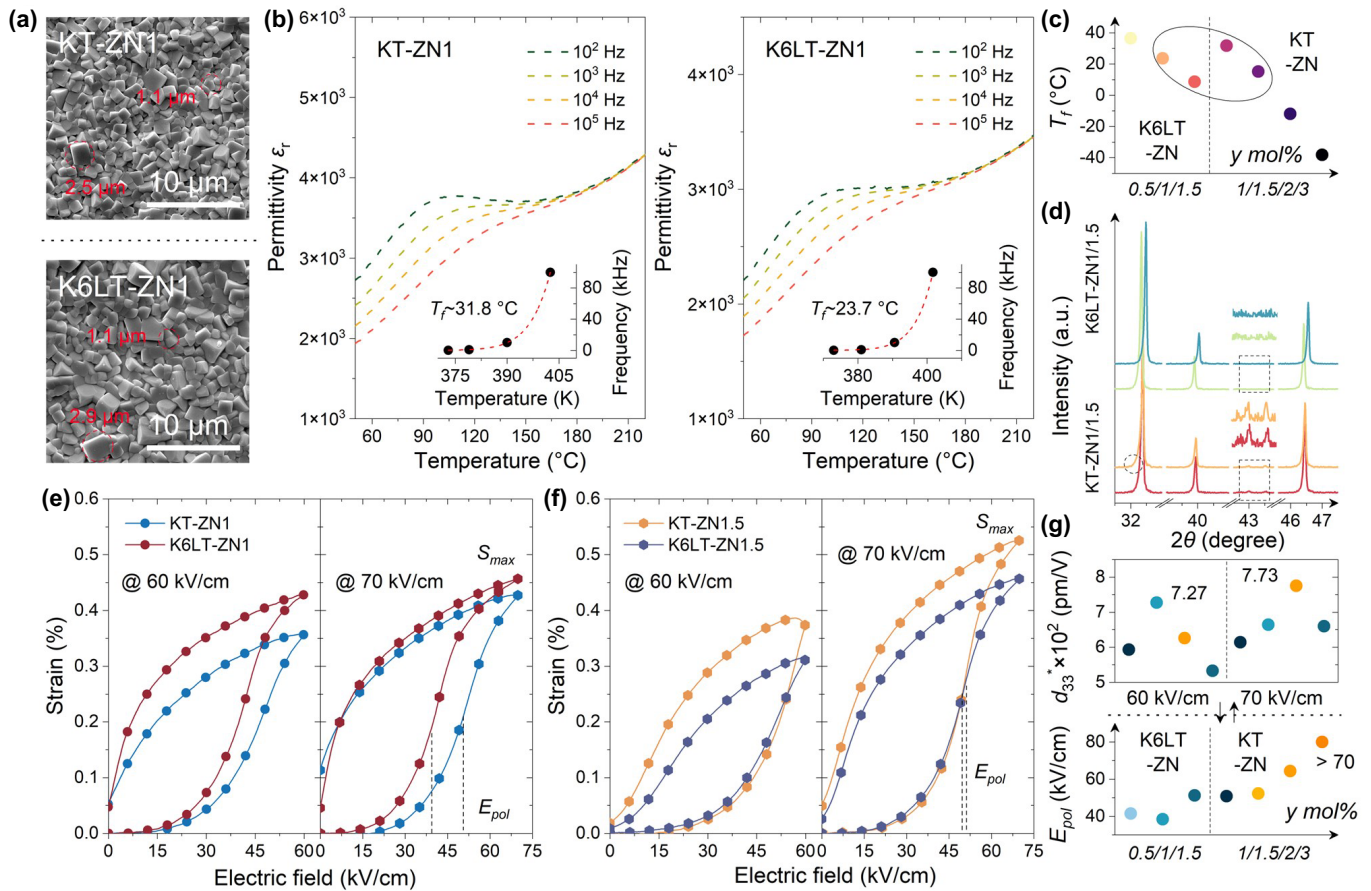


FIG. 4. (a) SEM images of KT-ZN1 and K6LT-ZN1 samples. (b) Dielectric curves (ϵ_r - T) with the inset of Vogel-Fulcher simulation. (c) Freezing temperature of KT-ZN100 y ($y = 0.01, 0.015, 0.02$ and 0.03) and K6LT-ZN100 y ($y = 0.005, 0.01$ and 0.015). (d) X-ray-diffraction patterns of KT (K6LT)-ZN1 (1.5). (e), (f) Strain properties of KT (K6LT)-ZN1 and KT (K6LT)-ZN1.5 under testing electric fields of 60 (70) kV/cm. (g) Large-signal piezoelectric coefficients and poling fields of KT-ZN100 y ($y = 0.01, 0.015, 0.02$ and 0.03) and K6LT-ZN100 y ($y = 0.005, 0.01$ and 0.015).

maintain most of its function for improving the polarization rotation, which is the essence for a phase transition process. Moreover, it can be found that for the second control group, even if K6LT-ZN1.5 exhibits a lower freezing temperature ($T_f \sim 8.7^\circ\text{C}$) than KT-ZN1.5 ($T_f \sim 15.2^\circ\text{C}$), the lower poling field (E_{pol} of K6LT-ZN1.5 ~ 51.2 kV/cm; KT-ZN1.5 ~ 52.4 kV/cm) is still observed in K6LT-ZN1.5, further confirming the partially retentive excellent MPB frame under small doping contents ($y = 0.01$ and 0.015) and the reliability of the proposed design guideline for giant-strain BNT-based systems (i.e., (i) screening the BNT matrix with an excellent MPB frame, and then (ii) regulating the T_d based on the screened BNT matrix).

The significance of optimizing the initial MPB frame for designing giant BNT-based has been revealed, and next, we will illustrate the reasons for strain-level evolution, especially for some unexpected phenomena (e.g., the decreased strain discrepancy $d_{33@70}^*$ between KT-ZN1 and K6LT-ZN1). Actually, poling-field levels regulate strain performances *via* relaxor-ferroelectric transition degree (e.g., complete phase transition and incomplete phase transition), and strain performances are dominated by lattice

discrepancies between the initial relaxor state and eventually ferroelectric state, in essence. Note that the eventually ferroelectric state should involve two parts: (i) the critical ferroelectric state (i.e., the ferroelectric state is just established with the coalesced polar entities) and (ii) the field-induced further growth of critical ferroelectric state (electrostriction effect). For the first control group, the driving energy from the relatively low external electric field (60 kV/cm) can only trigger the complete relaxor-ferroelectric transition of K6LT-ZN1 due to the low poling field caused by maintaining a decent MPB frame, and so the $d_{33@60}^*$ of K6LT-ZN1 is significantly enhanced compared with that of KT-ZN1. When the external electric field increases to 70 kV/cm, which can supply the sufficient driving energy for the phase transition process of both K6LT-ZN1 and KT-ZN1, strain performances should be determined by lattice discrepancies between the initial relaxor state and eventual field-triggered ferroelectric state. In more detail, considering the weak strain contribution from electrostriction effect, the crucial factor for strain performances should only be lattice discrepancies between the initial relaxor state and critical ferroelectric state (the critical ferroelectric state here should locate around the poling-field position), once the phase

transition is completely triggered under a large external field or samples present close poling-field levels. The *in situ* permittivity variation (from zero field to poling field) is utilized to qualitatively evaluate the lattice discrepancies and upper limit for strain levels. The larger *in situ* permittivity variation of KT-ZN1 gives the evidence for the larger lattice discrepancies (Fig. S13 [27]), and so it can be predicted that the strain discrepancy of $d_{33@70}^*$ between KT-ZN1 and K6LT-ZN1 will decline, conforming to experimental results (i.e., KT-ZN1 and K6LT-ZN1 exhibit the close $d_{33@70}^*$ values). For the second control group, KT-ZN1.5 and K6LT-ZN1.5 present the close poling-field level (E_{pol} of K6LT – ZN1.5 \sim 51.2 kV/cm; E_{pol} of KT – ZN1.5 \sim 52.4 kV/cm) but an evidently discrepant strain level; for instance, the $d_{33@70}^*$ of KT-ZN1.5 can even reach 773 pm/V, while it is only 660 pm/V for K6LT-ZN1.5. These should also be caused by different lattice discrepancies between the relaxor and ferroelectric states (Fig. S14), and in a sense, the initial relaxor structure discrepancies [Fig. 4(d)] between KT-ZN1 and K6LT-ZN1 or KT-ZN1.5 and K6LT-ZN1.5 may have implied some unpredictable circumstances about the strain level.

Overall, these interesting phenomena reflect an essential question for BNT-based strain performances, that is, what should be the practical demand of strain performances for BNT-based systems: low driving field with excellent strain level or high driving field with ultralarge strain level? From the perspective of practical applications, BNT-based systems with low driving field and excellent strain level should be appropriate due to the generally restricted external driving voltage. From the perspective of materials design, it is difficult to directly predict the lattice discrepancies between the initial relaxor state and eventual field-triggered ferroelectric state. As a result, declining the driving field by optimizing the MPB frame of initial BNT matrix is the better mode to improve strain performances.

III. CONCLUSIONS

Herein, by understanding the potential correlation between strain performance and phase boundary characteristics, we have established a comprehensive guideline for designing systems based on BNT with exceptional strain capabilities. This guideline entails the selection of an appropriate BNT matrix with a high-quality MPB framework, followed by the regulation of the transition temperature of the selected BNT matrix through the random-field effect. The MPB frame of the initial BNT matrix is found to have a close correlation with the final strain performances. In detail, when introducing a bit of doping components to regulate the transition temperature, an optimal initial MPB frame can maintain most of its function for improving the polarization rotation. The improved polarization rotation will directly accelerate the phase transition process by reducing the driving field, and then the excellent strain performances can be observed. The K6LT-ZN1 exhibits a low poling field E_{pol} of 38.4 kV/cm and high large-signal piezoelectric coefficient $d_{33@60}^*$ of 727 pm/V. Under the same condition, the $d_{33@60}^*$ of KT-ZN1 only reaches 583 pm/V due to the high driving field ($E_{\text{pol}} \sim$ 50.2 kV/cm). In summary, this proposed design concept devotes to improve strain performances by declining the driving field, and, whatever the perspective of practical application or materials design, the optimization of the initial MPB frame to regulate the driving field is a feasible approach.

The data corresponding to this study are available from the first author and corresponding authors upon request.

ACKNOWLEDGMENT

The authors acknowledge the support of the National Natural Science Foundation of China (Grants No. U23A20567 and No. 51972215).

-
- [1] W. Jo, R. Dittmer, M. Acosta, J. Zang, C. Groh, E. Sapper, K. Wang, and J. Rödel, Giant electric-field-induced strains in lead-free ceramics for actuator applications - status and perspective, *J. Electroceram.* **29**, 71 (2012).
 - [2] H. Wu, Y. Zhang, J. Wu, J. Wang, and S. J. Pennycook, Microstructural origins of high piezoelectric performance: A pathway to practical lead-free materials, *Adv. Funct. Mater.* **29**, 1902911 (2019).
 - [3] P. Fan *et al.*, Progress and perspective of high strain NBT-based lead-free piezoceramics and multilayer actuators, *J. Materiomics* **7**, 508 (2021).
 - [4] X. Wu, L. Wen, C. Wu, X. Lv, J. Yin, and J. Wu, Insight into the large electro-strain in bismuth sodium titanate-based relaxor ferroelectrics: From fundamentals to regulation methods, *J. Mater. Sci. Technol.* **150**, 27 (2023).
 - [5] X. Wu, C. Wu, L. Wen, J. Yin, and J. Wu, Unraveling the discrepancy of temperature- and composition-dependent strain regulation in $\text{Bi}_{0.5}\text{Na}_{0.5}\text{TiO}_3$ ceramics, *Appl. Phys. Lett.* **122**, 052901 (2023).
 - [6] C. W. Ahn *et al.*, A brief review on relaxor ferroelectrics and selected issues in lead-free relaxors, *J. Korean Phys. Soc.* **68**, 1481 (2016).
 - [7] J. Hao, W. Li, J. Zhai, and H. Chen, Progress in high-strain perovskite piezoelectric ceramics, *Mater. Sci. Eng., R* **135**, 1 (2019).
 - [8] J. Janbua, S. Niemchareon, R. Muanghlua, and N. Vittayakorn, High strain response of the $(1-x)(0.94\text{Bi}_{0.5}\text{Na}_{0.5}\text{TiO}_3 - 0.06\text{BaTiO}_3)$ - $x\text{BaSnO}_3$ lead free piezoelectric ceramics system, *Ferroelectrics* **490**, 13 (2016).
 - [9] J. U. Rahman, A. Hussain, A. Maqbool, T. K. Song, W. J. Kim, S. S. Kim, and M. H. Kim, Dielectric, ferroelectric and field-induced strain response of lead-free BaZrO_3 -modified $\text{Bi}_{0.5}\text{Na}_{0.5}\text{TiO}_3$ ceramics, *Curr. Appl Phys.* **14**, 331 (2014).
 - [10] G. Viola, T. Saunders, X. Wei, K. B. Chong, H. Luo, M. J. Reece, and H. Yan, Contribution of piezoelectric effect, electrostriction and ferroelectric/ferroelastic switching to strain-electric field response of dielectrics, *J. Adv. Dielectr.* **03**, 1350007 (2013).

- [11] D. S. Keeble, E. R. Barney, D. A. Keen, M. G. Tucker, J. Kreisel, and P. A. Thomas, Bifurcated polarization rotation in bismuth-based piezoelectrics, *Adv. Funct. Mater.* **23**, 185 (2013).
- [12] F. Li, S. Zhang, D. Damjanovic, L. Q. Chen, and T. R. Shrout, Local structural heterogeneity and electromechanical responses of ferroelectrics: Learning from relaxor ferroelectrics, *Adv. Funct. Mater.* **28**, 1801504 (2018).
- [13] X. Zhou, G. Xue, H. Luo, C. R. Bowen, and D. Zhang, Phase structure and properties of sodium bismuth titanate lead-free piezoelectric ceramics, *Prog. Mater. Sci.* **122**, 100836 (2021).
- [14] Y. Hiruma, H. Nagata, and T. Takenaka, Phase diagrams and electrical properties of $(\text{Bi}_{1/2}\text{Na}_{1/2})\text{TiO}_3$ -based solid solutions, *J. Appl. Phys.* **104**, 124106 (2008).
- [15] G. Das Adhikary, D. Sharma, P. Punetha, G. Jafo, G. Abebe, A. Mishra, A. Senyshyn, and R. Ranjan, Preponderant influence of disordered P4bm phase on the piezoelectricity of critical compositions of $\text{Na}_{0.5}\text{Bi}_{0.5}\text{TiO}_3$ -based ferroelectrics, *Phys. Rev. B* **104**, 184102 (2021).
- [16] I. Levin, I. M. Reaney, E. M. Anton, W. Jo, J. Rödel, J. Pokorny, L. A. Schmitt, H. J. Kleebe, M. Hinterstein, and J. L. Jones, Local structure, pseudosymmetry, and phase transitions in $\text{Na}_{1/2}\text{Bi}_{1/2}\text{TiO}_3 - \text{K}_{1/2}\text{Bi}_{1/2}\text{TiO}_3$ ceramics, *Phys. Rev. B* **87**, 024113 (2013).
- [17] H. Yan, F. Inam, G. Viola, H. Ning, H. Zhang, Q. Jiang, T. Zeng, Z. Gao, and M. J. Reece, The contribution of electrical conductivity, dielectric permittivity and domain switching in ferroelectric hysteresis loops, *J. Adv. Dielectr.* **01**, 107 (2011).
- [18] T. Li *et al.*, High-performance strain of lead-free relaxor-ferroelectric piezoceramics by the morphotropic phase boundary modification, *Adv. Funct. Mater.* **32**, 2202307 (2022).
- [19] H. Fu and R. E. Cohen, Polarization rotation mechanism for ultrahigh electromechanical response in single-crystal piezoelectrics, *Nature (London)* **403**, 281 (2000).
- [20] L. Zhang, H. Wang, D. Wang, M. Guo, X. Lou, and D. Wang, A new strategy for large dynamic piezoelectric responses in lead-free ferroelectrics: The relaxor/morphotropic phase boundary crossover, *Adv. Funct. Mater.* **30**, 2004641 (2020).
- [21] Z. Wang, D. Xiao, J. Wu, M. Xiao, F. Li, and J. Zhu, New lead-free $(1-x)(\text{K}_{0.5}\text{Na}_{0.5})\text{NbO}_{3-x}(\text{Bi}_{0.5}\text{Na}_{0.5})\text{ZrO}_3$ ceramics with high piezoelectricity, *J. Am. Ceram. Soc.* **97**, 688 (2014).
- [22] J. Xing, Z. Tan, X. Chen, L. Jiang, W. Wang, X. Deng, B. Wu, J. Wu, D. Xiao, and J. Zhu, Rietveld analysis and electrical properties of BiInO_3 doped KNN-based ceramics, *Inorg. Chem.* **58**, 428 (2019).
- [23] J. Xing, Z. Tan, J. Yuan, L. Jiang, Q. Chen, J. Wu, W. Zhang, D. Xiao, and J. Zhu, Structure and electrical properties of $(0.965-x)(\text{K}_{0.48}\text{Na}_{0.52})\text{NbO}_3 - x\text{BiGaO}_3 - 0.035(\text{Bi}_{0.5}\text{Na}_{0.5})\text{ZrO}_3$ piezoelectric ceramics, *RSC Adv.* **6**, 57210 (2016).
- [24] Y. Yan, K. H. Cho, and S. Priya, Piezoelectric properties and temperature stability of Mn-doped $\text{Pb}(\text{Mg}_{1/3}\text{Nb}_{2/3})\text{-PbZrO}_3 - \text{PbTiO}_3$ textured ceramics, *Appl. Phys. Lett.* **100**, 132908 (2012).
- [25] H. Zhang, J. Zhou, J. Shen, W. Jin, J. Zhou, and W. Chen, High-field nonlinear properties and characteristics of domain wall motion in Fe_2O_3 doped PMnS-PZN-PZT ceramics, *Ferroelectrics* **560**, 110 (2020).
- [26] M. Waqar, H. Wu, J. Chen, K. Yao, and J. Wang, Evolution from lead-based to lead-free piezoelectrics: Engineering of lattices, domains, boundaries, and defects leading to giant response, *Adv. Mater.* **34**, 2106845 (2021).
- [27] See Supplemental Material at <http://link.aps.org/supplemental/10.1103/PhysRevMaterials.8.034406> for the detailed experiments; x-ray and SEM characterization of the samples; dielectric curves with calculated freezing temperatures of the samples; ferroelectric hysteresis and strain-rate loops of the samples; Raman spectra and simulated results of KT, K6LT and K15LT samples; and *in situ* permittivity evolution of KT (K6LT)-ZN1 (1.5) samples.
- [28] B. Wu, J. Ma, W. Wu, and M. Chen, Improved piezoelectricity in ternary potassium-sodium niobate lead-free ceramics with large strain, *J. Mater. Chem. C Mater* **8**, 2838 (2020).
- [29] S. T. Zhang, A. B. Kouna, E. Aulbach, H. Ehrenberg, and J. Rödel, Giant strain in lead-free piezoceramics $\text{Bi}_{0.5}\text{Na}_{0.5}\text{TiO}_3 - \text{BaTiO}_3 - \text{K}_{0.5}\text{Na}_{0.5}\text{NbO}_3$ system, *Appl. Phys. Lett.* **91**, 112906 (2007).
- [30] M. Kroutvar, Y. Ducommun, D. Heiss, M. Bichler, D. Schuh, G. Abstreiter, and J. J. Finley, Optically programmable electron spin memory using semiconductor quantum dots, *Nature (London)* **432**, 81 (2004).
- [31] M. H. Lee, D. J. Kim, J. S. Park, S. W. Kim, T. K. Song, M. H. Kim, W. J. Kim, D. Do, and I. K. Jeong, High-performance lead-free piezoceramics with high curie temperatures, *Adv. Mater.* **27**, 6976 (2015).
- [32] J. Schultheiß, G. Picht, J. Wang, Y. A. Genenko, L. Q. Chen, J. E. Daniels, and J. Koruza, Ferroelectric polycrystals: Structural and microstructural levers for property-engineering via domain-wall dynamics, *Prog. Mater. Sci.* **136**, 101101 (2023).
- [33] A. Pramanick, D. Damjanovic, J. E. Daniels, J. C. Nino, and J. L. Jones, Origins of electro-mechanical coupling in polycrystalline ferroelectrics during subcoercive electrical loading, *J. Am. Ceram. Soc.* **94**, 293 (2011).
- [34] F. Li, L. Jin, Z. Xu, and S. Zhang, Electrostrictive effect in ferroelectrics: An alternative approach to improve piezoelectricity, *Appl. Phys. Rev.* **1**, 011103 (2014).
- [35] M. Otonicar, M. Dragomir, and T. Rojac, Dynamics of domain walls in ferroelectrics and relaxors, *J. Am. Ceram. Soc.* **105**, 6479 (2022).
- [36] M. Otoničar *et al.*, Connecting the multiscale structure with macroscopic response of relaxor ferroelectrics, *Adv. Funct. Mater.* **30**, 2006823 (2020).
- [37] L. M. Riemer, L. Jin, H. Uršič, M. Otonicar, T. Rojac, and D. Damjanovic, Dielectric and electro-mechanic nonlinearities in perovskite oxide ferroelectrics, relaxors, and relaxor ferroelectrics, *J. Appl. Phys.* **129**, 054101 (2021).
- [38] P. Peng, H. Nie, Z. Liu, G. Wang, X. Dong, Y. Zhang, C. Duan, and X. Tang, Scaling behavior for $(\text{Bi}_{0.5}\text{Na}_{0.5})\text{TiO}_3$ based lead-free relaxor ferroelectric ceramics, *J. Appl. Phys.* **122**, 064102 (2017).
- [39] B. Pan, H. Yu, D. Wu, X. H. Zhou, and J. M. Liu, Dynamic response and hysteresis dispersion scaling of ferroelectric $\text{SrBi}_2\text{Ta}_2\text{O}_9$ thin films, *Appl. Phys. Lett.* **83**, 1406 (2003).
- [40] R. Yimnirun, Y. Laosiritaworn, S. Wongsanmai, and S. Ananta, Scaling behavior of dynamic hysteresis in soft lead zirconate titanate bulk ceramics, *Appl. Phys. Lett.* **89**, 162901 (2006).

- [41] D. Schütz, M. Deluca, W. Krauss, A. Feteira, T. Jackson, and K. Reichmann, Lone-pair-induced covalency as the cause of temperature- and field-induced instabilities in bismuth sodium titanate, *Adv. Funct. Mater.* **22**, 2285 (2012).
- [42] Y. Yoneda, T. Kobayashi, T. Tsuji, D. Matsumura, Y. Saitoh, and Y. Noguchi, Local structure analysis of $\text{Bi}_{0.5}\text{Na}_{0.5}\text{TiO}_3$ – BaTiO_3 solid solutions, *Jpn. J. Appl. Phys.* **62**, SM1006 (2023).